A Stage–Stage Dead-Band Compensated Multiband RF Energy Harvester for Sensor Nodes

S. Nagaveni, Sesha Sairam Regulagadda, and Ashudeb Dutta, *Member, IEEE*

***Abstract*—This article presents a dead-band compensated multiband stacked electromagnetic energy harvester for powering sensor nodes. It is adaptive for typical ambient radio frequency (RF) power levels found within the environment. A stage–stage feedforward technique is adopted in the proposed harvester to enhance the output voltage, in turn, harvested power and sensitivity. Moreover, a compensation circuit is included in the design for bypassing the inactive bands to avoid unexcited band rectifier diodes. A prototype is designed to cover four frequency bands GSM (900 and 1800 MHz), 4G-LTE (2.3 GHz), and Wi-Fi (2.4 GHz) and further integrated with a TI BQ25570 power converter. The analytical, simulated, and measured results show the increment in the output voltage with the frequency bands. The measured efficiency of the RF-to-dc converter is 44.2% at −20-dBm input power and 89% at 0 dBm. The efficiency is improved by 13% on average under dead-band compensation. With the multiband stacking, the harvester achieves a start-up voltage of 320 mV at −24 dBm and is found to be efficient to drive a temperature sensor STLM20 at −12-dBm input power.**

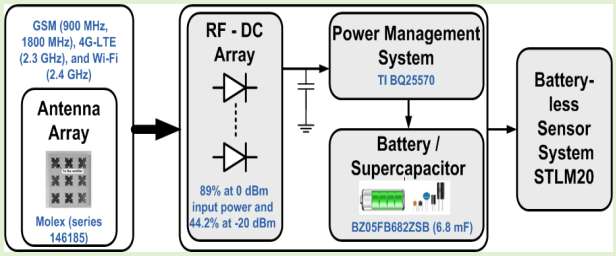

***Index Terms*— Dead band, impedance matching network, multiband, power management, radio frequency (RF) energy harvesting, rectifier.**

I. Introduction

RECENTLY, radio frequency (RF) waves are pervasive in our ambient environment due to the development of multiple wireless communication technologies, such as TV, radio, cellular, wireless local area network (WLAN), and Wi-Fi. Therefore, powering electronic devices through electromagnetic energy harvesting will be future demand. On the other hand, the power consumption of some sensors and RFID decreased to the microwatt level with the progress in integrated circuit technology. The drawback of RF energy scavenging is that the power density that they can provide is low (0.01–0.1 μW/cm^2) [1] compared to the photovoltaic (10–10 mW/cm^2) or thermal (20–10 mW/cm^2) ones [2]. However, the advantage of RF energy is ubiquitous in the environment and spread over a wide frequency range. Fig. 1(a) shows the power density of electromagnetic waves in the ambient condition (power spectrum of an inverted F antenna from Molex, series 146185 is given in Appendix). It outlines the received average power levels in an office environment during weekdays at GSM900, GSM1800, 4G-LTE (2.3 GHz), and Wi-Fi (2.4 GHz) are −30, −35, −23, and −20 dBm, respectively. Hence, developing harvesters to harvest all the potential RF energy present in the environment at these unused bands can help to increase the autonomy of wireless objects.

Preliminary works with RF energy harvester (RF-EH) circuits concentrated on harvesting power at single operating frequency [3], [4], [5]. As multiple potential RF sources are present, the harvested power can be increased by designing a system to work at all potential frequency bands. The gradual enhancement of dc output voltage of an RF-EH under multiple-frequency signals scavenging scenarios is shown in Fig. 1(b). Hence, the multiband [6] or wideband [7] energy harvesting is preferred over single band.

A few works have been done on tunable harvesting [8], wideband harvesting [7], and multiband harvesting [6], [9], [10], [11], [12]. However, wideband harvester tries to harvest over a large spectrum, typically resulting in low efficiency

Manuscript received 6 December 2022; revised 8 January 2023; accepted 10 January 2023. Date of publication 23 January 2023; date of current version 28 February 2023. The associate editor coordinating the review of this article and approving it for publication was Dr. Yongjia Li. *(Corresponding author: S. Nagaveni.)*

S. Nagaveni is with the Department of Electrical Engineering, Indian Institute of Technology Dharwad, Dharwad 580011, India (e-mail: nagaveni@iitdh.ac.in).

Sesha Sairam Regulagadda is with Silicon Labs, Hyderabad 500081, India (e-mail: ee14resch11013@iith.ac.in).

Ashudeb Dutta is with the Department of Electrical Engineering, Indian Institute of Technology Hyderabad, Hyderabad 502285, India (e-mail: asudeb_dutta@iith.ac.in).

Digital Object Identifier 10.1109/JSEN.2023.3237544

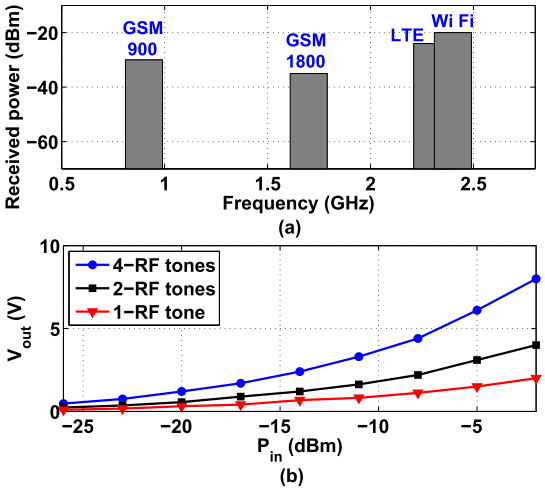

Fig. 1. (a) Received RF power using an immobile R&S FSW50 spectrum analyzer and a wideband antenna with a gain of 5 dBi. (b) Impact on dc output voltage due to multifrequency signals. Considered two-stage Dickson-based rectifier [Fig. 5(b)] for simulation.

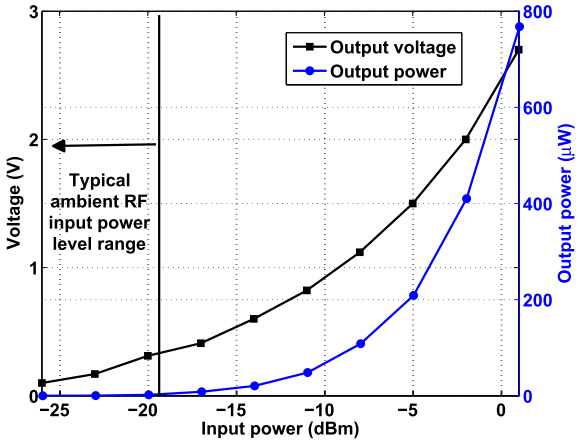

Fig. 2. Simulated output voltage and output power of a two-stage rectifier at 900 MHz.

due to the reduction of quality factor (Q) of the impedance matching network with the increase of bandwidth [7]. In contrast, tunable harvesting system [8] selects the desired band depending on the spectral availability, hence providing efficient performance at a single frequency, regardless of the source frequency with the demand of start-up circuit.

The reported prior art multiband harvesting kinds of literature are [6], [9], [10], [11], and [12]. The works [9] and [10] are focused on the design of improved rectifier to operate over a wide response power range, whereas studies [6] and [11] worked on the improvement of an output voltage through combining multifrequency signals via multiresonator matching network and multipath stacking, respectively. A novel eight-band rectenna (0.84, 1.29, 1.68, 108 3.08, 3.45, 4.31, 5.11, and 5.49 GHz) was proposed in [27] by designing an eight-band matching network within a single branch. However, the RF-to-dc conversion efficiency was only 13.5%, 3.3%, and 12.68% at 4.31, 5.11, and 5.49 GHz, respectively, at an input power of 10 dBm due to poor matching performance. The works [9] and [10] show the efficiency of >30% from −15 to 20 dBm and −12 to 12 dBm, respectively, whereas works [6] and [11] present an efficiency of 15% at −20 and −13 dBm, respectively. However, these topologies, in the context of multifrequency harvesting, impart high efficiency only when all frequency bands are excited (bands are excited only when a minimum power to harvest is available). The diode drops in the unexcited bands are overcome by the other band, resulting in significant efficiency degradation. The literature [12] shows an efficiency of 15% at −12 dBm; however, in this architecture, each RF band chain requires an individual power management module (PMM), which leads to more power consumption and form factor. With this, a modified stacking rectifier with improved sensitivity (minimum source power that is feasible to harvest) and a dead-band compensation (DBC) stage is proposed.

The contributions of this article are given as follows: 1) stage–stage stacking of rectifier for dc combining; 2) diode structure to bypass the inactive band; 3) analytical model for an output voltage of rectifier stacking; and 4) interfacing of rectifier stacking with PMM and observed the charging profile of the supercapacitor.

This article is organized as follows. Section II describes the challenges in single-band and multiband energy harvesters (EHs). The proposed architecture and critical building blocks are discussed in Section III. Finally, Section IV shows the measurement results for the RF energy harvesting systems, followed by a conclusion in Section V.

II. Overview of RF Energy Harvesting

A typical RF-EH system consists of an antenna to receive the electromagnetic energy followed by an impedance matching network for maximum power transfer and passive voltage boosting. The next building block is the rectifier for RF-to-dc conversion. In this design, a Schottky-based rectifier is considered because of its low threshold voltage (∼150 mV). In addition, the output of the rectifier is fed to the PMM to raise the output voltage to the required value for driving an application. The following discusses the limitation of the single-band EH and the prior multiband EH topologies.

A. Challenges in a Single-Band EH

The prior art on single-band EH [3] shows the output power of 10 μW for −10-dBm input power level at 914 MHz. Mikeka et al. [5] claimed the harvested power of 1.8 μW for −20 dBm at 550 MHz. However, the harvested voltage and power are insufficient to drive a sensor node (Table I) at typical ambient RF power levels (e.g., -23 ± 3 dBm). This can be observed from the simulated results of single-band two-stage Dickson-based RF-EH, as shown in Fig. 2. Also, the performance of such harvesters degrades with the change of operating frequency from the resonance frequency. Another way to increase the output power is by increasing source power, but the maximum transmit source power (30 dBm) at industrial, scientific and medical (ISM) bands is restricted by the Federal Communications Commission.

B. Challenges in a Multiband EH

To address the challenges in single-band energy harvesting, several multiband array architectures are investigated in

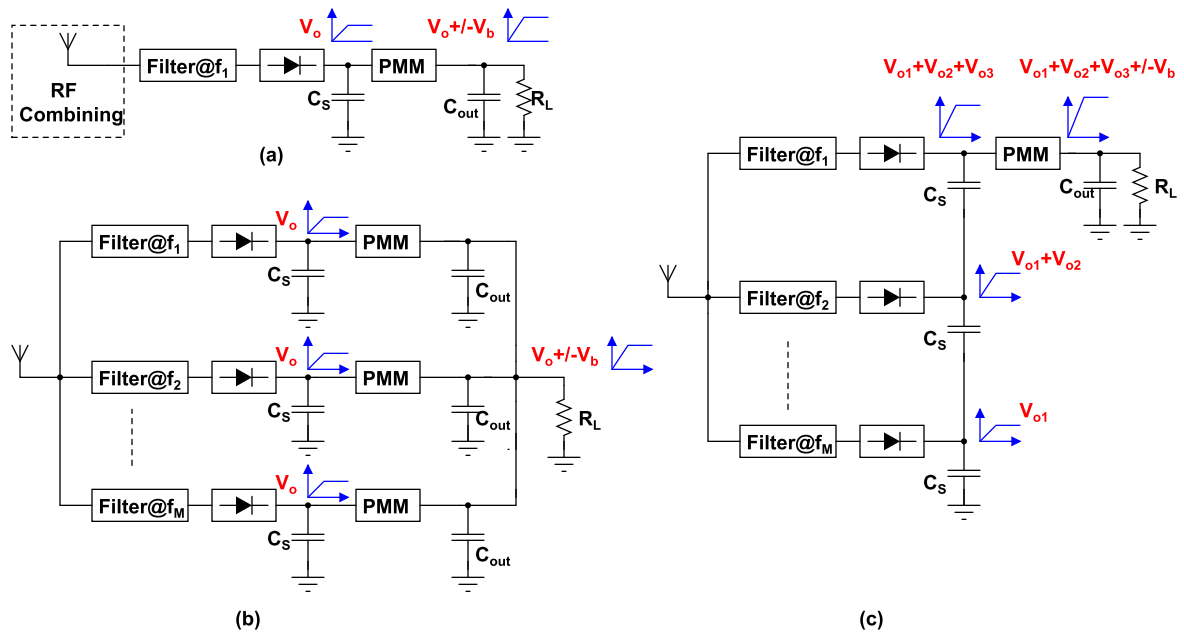

Fig. 3. Multiband RF harvester architectures. (a) Single RF chain with RF combining at an antenna. (b) Multiple RF chain with multiple PMMs. (c) Proposed architecture. ($+V_b$/$-V_b$ represent the boost/buck voltages, respectively.)

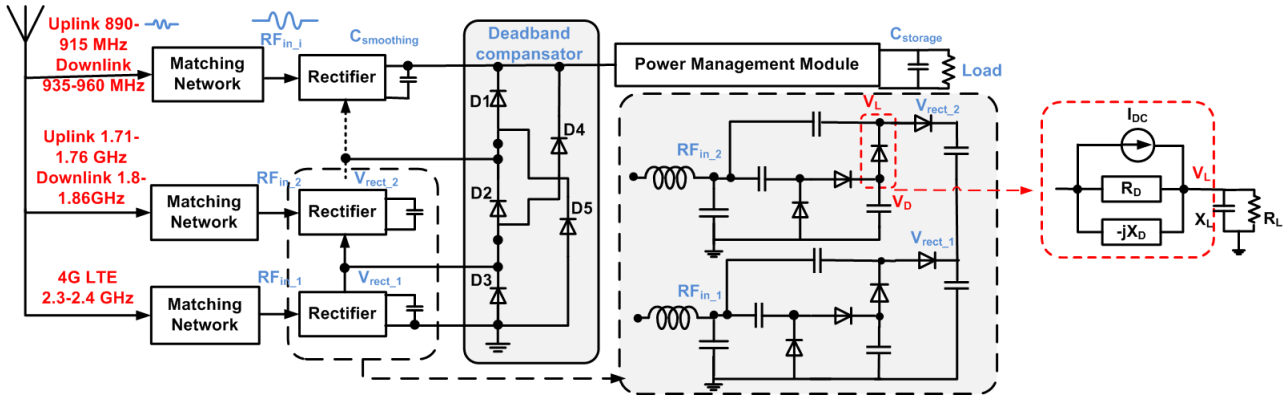

Fig. 4. Proposed architecture with rectifier circuit.

TABLE I
TYPICAL SENSOR INFORMATION

Sensor	STLM20 [23]	MS8607 -02BA01 [24]	TSYS02D [25]
DC supply (V)	2.4-5.5	3.6	3.6
Max current (μA)	4.8	20	420

which multiple-frequency bands are targeted simultaneously to increase the output voltage and power. The first way of multiband energy harvesting is RF power combining, which merges the incoming signal from multiple antennas in front of the rectifier, as shown in Fig. 3(a). However, it demands the RF power combiner structure that employs coherent reception of incoming signals [14], [15], [16]. The second way is dc combining [6], [17], [18] in which the output of the rectifier or the output of PMM is connected in parallel. Fig. 3(b) shows the dc combining at the PMM output. It incorporates multiple RF chains (each RF chain includes an antenna, impedance matching network, and rectifier) with individual PMM. On the other hand, this topology is not suitable for low input power levels. It requires a minimum voltage at every chain of rectifier output to kick-start their respective PMMs. The dc combining at the output of the rectifier causes unbalance (high output voltage branch dominates the low output voltage branch) in the architecture due to a variation of rectifier output voltage since the RF chains are operating at different frequencies. To tackle this, a proposed stage–stage feedforward stack rectifier is given in Fig. 3(c), in which the output of the rectifier increments with the number of bands sequentially reduces the start-up voltage for PMM and is hence suitable for low input power scenarios.

In most actual use cases, all frequency bands in the radio spectrum are not present at all times and every location. The power density received by the RF bands will vary with each other since they are operating at different frequencies. The unavailability of RF power at any operating frequency will inactivate the particular RF chain. This inactive band will create an obstacle to the current flow from the excited

TABLE II
MATCHING NETWORK COMPONENT VALUES

RF chain	Freq. (GHz)	C_L (pF)	L_S (nH)	C_R (pF)
V_{in_1}	0.9	2.74	24.5	1.46
V_{in_2}	1.8	0.9	11.9	0.73
V_{in_3}	2.3	0.7	9.2	0.57
V_{in_4}	2.4	0.67	8.9	0.54

bands, which in turn hinders the system performance in the series connection. To gear this problem, bypass switches are placed around individual RF chain. Further details are given in Section III-B.

III. ARCHITECTURE OF MULTIBAND EH

The proposed architecture in Figs. 3(c) and 4 is composed of multiple RF chains connected in stage–stage feedforward mode and each chain incorporates a matching network to select a specific frequency and an RF-to-dc converter. Furthermore, the design is interfaced with a TI-BQ25570 PMM to step up the rectifier output to a voltage level between 2.4 and 5.3 V to power up a temperature sensor.

A. Proposed Multiband Stage–Stage Feedforward Stack Rectifier

Fig. 5(a) shows the proposed stage–stage feedforward multiband rectifier in which a voltage doubler is chosen for RF-to-dc conversion due to a limited number of diodes. In this design, the output capacitor of the previous band (V_{in_1}) is fed to the output capacitor of the next band (V_{in_2}). This will effectively increase the output voltage measured with respect to ground. The increment in the output voltage of the proposed [Fig. 5(a)] structures with impedance matching is shown in Fig. 5(b). Also, the intermediate node voltage, current, and the harvested power are shown in Fig. 6. The observation from these plots is that the proposed topology outperforms in the presence of more than one band. In addition to avoid leakage from one chain to another chain, the DBC circuit is incorporated with the proposed rectifier chain. The DBC includes the diodes around the output nodes to bypass the RF chain with a low output voltage compared to others. Details about DBC are discussed in Section III-B.

1) Steady-State Analysis of Stage–Stage Multiband EH: The dynamics of the proposed rectifier is investigated in a steady state to calculate the output voltage. Let the RF input voltage be $V_{\text{in}} = V_{\text{RF}}\cos\omega t$, where V_{RF} is the peak voltage. The charges Q_1 and Q_3 stored in C_1 and C_3 at $t = T/2$ in Fig. 7 are given as

$$Q_1 = C_1(V_{\text{RF}_1} - V_{d_1}) \quad \text{Coulomb} \tag{1}$$

$$Q_3 = C_3(V_{\text{RF}_2} - V_{d_3} + V_{\text{rect}_1}) \quad \text{Coulomb} \tag{2}$$

where V_{d_1} and V_{d_3} are the voltage drop across the diode D_1 and D_3, respectively, and V_{rect_1} is the output voltage of

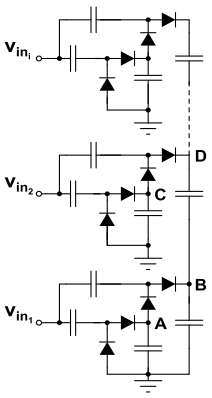

(a)

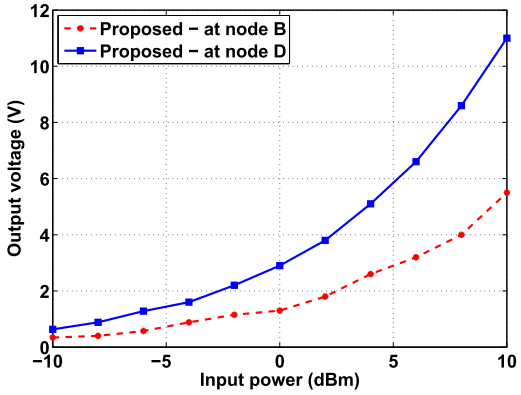

(b)

Fig. 5. (a) Stage–stage feedforward multiband rectifier schematic. (b) Rectifier output voltage with impedance matching at different nodes (Fig. 5) at $R_L = \infty$.

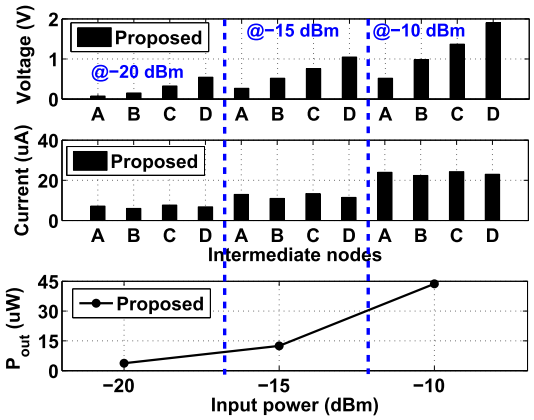

Fig. 6. Intermediate node voltage, current, and harvested power with impedance matching.

V_{in_1} input band. Also, the voltage across the diode D_2 is given as

$$V_{d_2} = \frac{Q_1}{C_1} + V_{\text{RF}_1} - \frac{Q_2}{C_2} \quad \text{Volt.} \tag{3}$$

Similarly, during a positive half cycle of the input signal (from $t = T/2$ to T), the charge Q_2 in C_2 is given as

$$Q_2 = C_2\left(V_{\text{RF}_1} - V_{d_2}\right) + Q_1 \quad \text{Coulomb.} \tag{4}$$

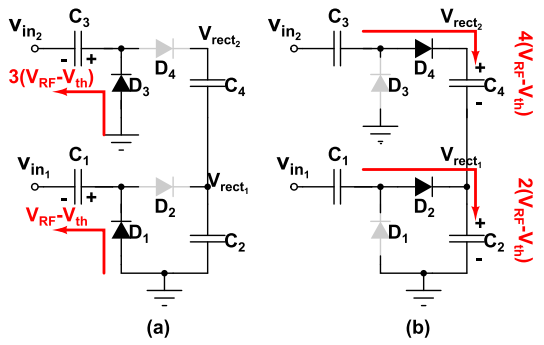

Fig. 7. Working operation of a stacked rectifier. (a) Negative half cycle ($t = 0$–$T/2$). (b) Positive half cycle ($t = T/2$ to T).

Let us consider $C_1 = C_2 = C_3 = C_4 = C$ and $V_{d_1} = V_{d_2} = V_{d_3} = V_{d_4} = V_{\text{th}}$

$$Q_2 = 2C\left(V_{\text{RF}_1} - V_{\text{th}}\right) \quad \text{Coulomb.} \tag{5}$$

The voltage across D_4 is shown as follows:

$$V_{d_4} = \frac{Q_3}{C} + V_{\text{RF}_2} - \frac{Q_4}{C} \quad \text{Volt} \tag{6}$$

$$Q_4 = C(V_{\text{RF}_2} - V_{d_4}) + Q_3 \quad \text{Coulomb} \tag{7}$$

$$Q_4 = 2C(V_{\text{RF}_2} - V_{th}) + CV_{\text{rect}_1} \quad \text{Coulomb.} \tag{8}$$

From (5), $V_{\text{rect}_1} = Q_2/C$ is represented as

$$V_{\text{rect}_1} = 2\left(V_{\text{RF}_1} - V_{th}\right) \quad \text{Volt.} \tag{9}$$

In general, Q_M is given as

$$Q_M = 2C\left(V_{\text{RF}_1} - V_{th}\right) + 2C\left(V_{\text{RF}_2} - V_{th}\right) + \cdots + 2C\left(V_{\text{RF}_M} - V_{th}\right) \quad \text{Coulomb} \tag{10}$$

where M is the number of bands. Similarly, V_{rect_M} is given as

$$V_{\text{rect}_M} = 2\left(V_{\text{RF}_1} - V_{th}\right) + 2\left(V_{\text{RF}_2} - V_{th}\right) + \cdots + 2\left(V_{\text{RF}_M} - V_{th}\right) \quad \text{Volt.} \tag{11}$$

The output voltage for N stage rectifier with M bands is given as

$$V_{\text{rect}_M} = \sum_{i=1}^{M} 2N\left(V_{\text{RF}_i} - V_{th}\right) = 2NM\left(V_{\text{RF}} - V_{th}\right) \quad \text{Volt.} \tag{12}$$

It is evident from (12) that the stage–stage topology will boost the output voltage as well as improve the input power sensitivity. The simulation result of the output voltage at the four-RF active band is four times higher than the output voltage of a one-RF active band at no-load condition, and it is highlighted in Fig. 8. Also, Fig. 9 confirms the correlation between the equation and simulation-based output voltage and shows the error percentage of <10% for input power range from −18 to −7 dBm.

Furthermore, in the proposed one, the performance degrades due to OFF-state diode drops in the unexcited bands. Therefore, a DBC is introduced in this design.

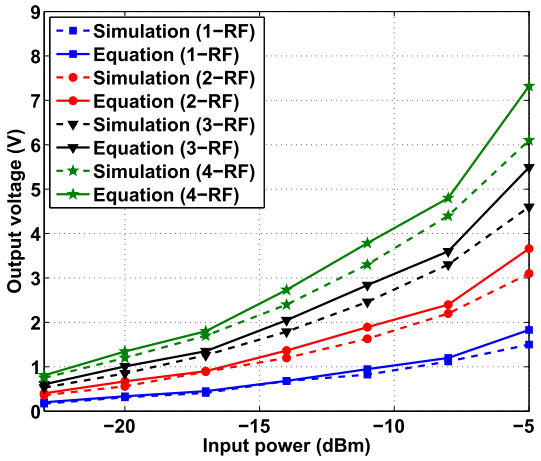

Fig. 8. Simulated and (12)-based dc output voltage as a function of input power. (V_{RF} is the peak voltage at the output of the matching network and is considered from the simulation.)

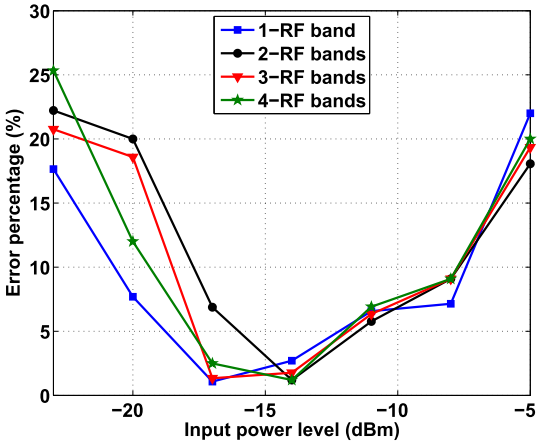

Fig. 9. Error percentage between simulation results and the values obtained from (12) as a function of input power.

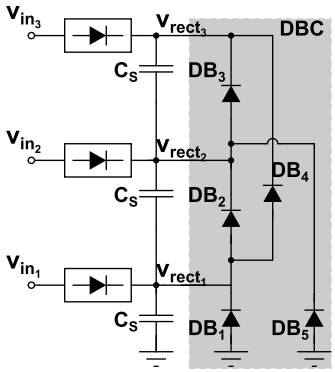

Fig. 10. DBC circuit.

B. Dead-Band Compensation

The DBC circuit is shown in Fig. 10, in which bypass switches are placed around each RF chain to overcome the unexcited band diode drops. The output voltage V_{rect_1} is fed as dc input to the V_{in_2} chain only when $V_{\text{rect}_2} > V_{\text{rect}_1}$ by reverse biasing the diode DB_2. If V_{in_2} band is unexcited and V_{in_1} is excited, then the output voltage V_{rect_1} is fed to the preceding chain (V_{in_3}) by forward biasing the diode DB_2.

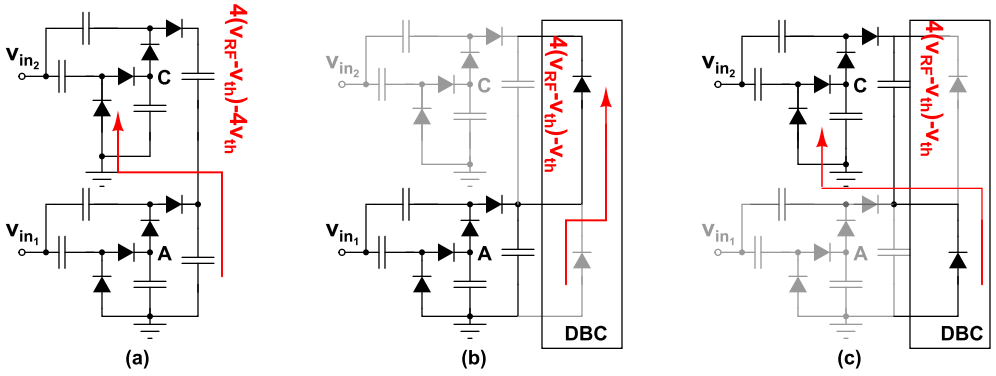

Fig. 11. (a) Without DBC (V_{in_1} = active and V_{in_2} = inactive), (b) with DBC (V_{in_1} = active and V_{in_2} = inactive), and (c) with DBC (V_{in_1} = inactive and V_{in_2} = active).

The output voltage of the rectifier stacking without DBC for P number of an inactive band is expressed as

$$V_{\text{rect}_M} = 2\ N\ (M - P)\ (V_{\text{RF}} - V_{th}) - 2\ PNV_{th} \quad \text{Volt} \quad (13)$$

where M is the number of frequency bands and N is the number of rectifier stages. Furthermore, the equation of the output voltage with the DBC is expressed as

$$V_{\text{rect}_M} = 2\ N\ (M - P)\ (V_{\text{RF}} - V_{th}) - V_{th} \quad \text{Volt.} \quad (14)$$

It is apparent from (13) and (14) that the impact of an inactive band is resolved with the DBC. Fig. 11 shows an example of with DBC and without DBC when V_{in_2} chain is unexcited and V_{in_1} chain is excited. The evidence from Fig. 11 is that the output voltage without DBC is $V_{\text{rect}_M} = 4(V_{\text{RF}} - V_{th}) - 4V_{th}$ with $4V_{th}$ of inactive rectifier diode drops and the output voltage with DBC is $V_{\text{rect}_M} = 4(V_{\text{RF}} - V_{th}) - V_{th}$ with single DBC diode drop.

C. Implementation of Matching Network

In an RF-EH system, besides delivery of maximum power from RF source to load, the impedance matching network also helps in improving the efficiency (the ratio of output power to source power) and sensitivity of an RF energy harvesting system. The power received by the matching network (P_{load}) is given by

$$P_{\text{load}} = P_{\text{avail}} \left(1 - \Gamma^2\right) \quad \text{Watt} \quad (15)$$

where Γ represents the reflection coefficient at the input of the matching network.

Typically, off-chip components and bond wires are preferred for matching networks in RF-EH systems due to high Q-factor (low loss) compared to on-chip components. The matching network functions as a passive voltage or current amplifier and, thus, in turn, increases the sensitivity of the RF-EH systems. In this design, a Pi-matching configuration is used as it has flexibility to vary the Q-factor, which in turn is useful in improving the passive voltage boost.

The component values of the Pi-matching network in Fig. 12(a) can be derived by splitting the network into two L-matching networks, as shown in Fig. 12(b). Let X_{L_R}, X_{L_L}, X_{C_R}, and X_{C_L} are the reactance of the inductors L_R and L_L

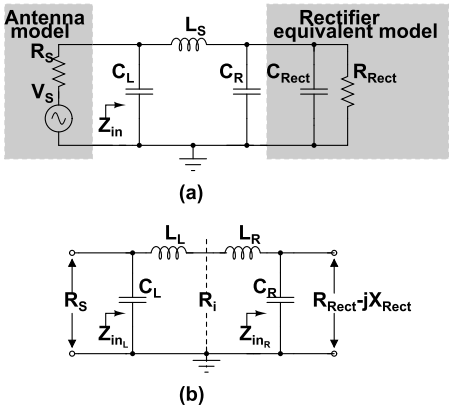

Fig. 12. (a) Pi-impedance matching network. (b) Cascade of two L-matching networks.

and capacitors C_R and C_L, respectively. Assume that ω is the desired frequency and Q_L and Q_c are the quality factor of the inductor and capacitor, respectively.

The impedance of the right-hand side L-matching in Fig. 12(b) is given as

$$Z_{\text{in}_R} = jX_{L_R} + \left(jX_{C_R} || \left(R_{\text{Rect}} + jX_{\text{Rect}}\right)\right) \quad \Omega \quad (16)$$

where $X_{L_R} = \omega L_R$, $X_{C_R} = -1/(\omega C_R)$, and $X_{\text{Rect}} = -1/(\omega C_{\text{Rect}})$.

The right-hand side L-network elements (L_R, C_R) are derived from (24) and (25) given in the Appendix by considering

$$\text{real}\left(Z_{\text{in}_R}\right) = R_i, \quad \text{imag}\left(Z_{\text{in}_R}\right) = 0 \quad (17)$$

where R_i is the intermediate resistance.

Similarly, by deriving $\text{real}(Z_{\text{in}_L}) = R_S$, $\text{imag}(Z_{\text{in}_L}) = 0$, the left-hand L-matching network values (L_L, C_L) are calculated from (26) and (27).

Here, Z_{in_L} is given as

$$Z_{\text{in}_L} = \left(R_i + jX_{L_L}\right) || jX_{C_R} \quad \Omega. \quad (18)$$

The calculated matching network values at $Q_L = 50$ and $Q_C = 100$ are shown in Table II. The inductor from Coilcraft (0402CS 4NS, 0402 11N) and the capacitor from Murata (GRM0222c1e1r0wa03 and GRM0222c1e2r8ba03) are chosen for validation.

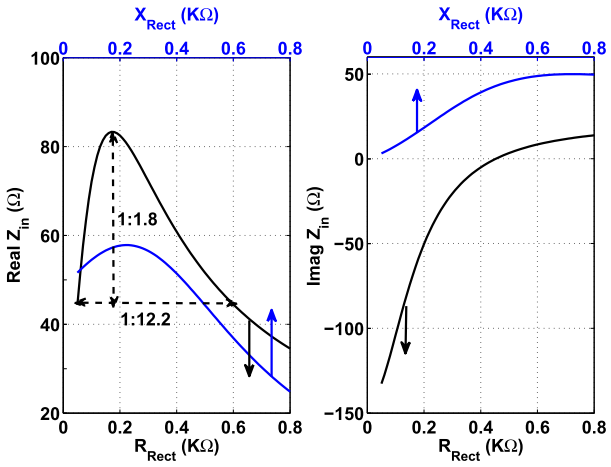

Fig. 13. (a) Variation of real impedance. (b) Imaginary impedance as a function of load.

1) Matching Network Impedance Variation Due to Stage–Stage Rectifier: In RF-EH, the rectifier impedance is sensitive toward the variation in input power level, frequency, and load. Furthermore, the variation in the rectifier impedance encounters the input impedance mismatch and degrades its performance. Besides, the dependence of rectifier impedance on its input power and frequency variation, in a multiband stacked array architecture, as the output of the previous band is fed as a dc input to the next band, which construct the dependence on the performance of the preceding band.

The impedance Z_{in} in Fig. 12(a) is given as follows:

$$Z_{\text{in}} = -jX_{C_L} \,||\, \left(jX_{L_S} + (R_{\text{Rect}} - jX_{\text{Rect}}) \,||\, \left(-jX_{C_R}\right)\right) \quad \Omega. \tag{19}$$

A simplified form of (19) is given as follows:

$$Z_{\text{in}} = \frac{A - jB}{C} \quad \Omega \tag{20}$$

where

$$A = R_{\text{Rect}} X_{C_L} \left(X_{L_S} - X_{C_R}\right) \tag{21}$$

$$B = X_{L_S} X_{C_L} X_{C_R} + X_{\text{Rect}} \tag{22}$$

$$C = X_{L_S} X_{C_R} - X_{C_L} X_{C_R} + X_{\text{Rect}} + jR_{\text{Rect}} \left(X_{L_S} - X_{C_L} - X_{C_R}\right). \tag{23}$$

The real and imaginary impedances of Z_{in} are plotted against the variation of rectifier impedance at an operating frequency of 900 MHz and also compared the ratio between the smallest and largest values of Z_{in} with the smallest and largest values of $R_{\text{Rect}} - jX_{\text{Rect}}$ variation. In Fig. 13(a), for an R_{Rect} range from 50 to 612 Ω (a ratio of 1:12.2), the real Z_{in} varies from 45 to 82 Ω (a ratio of 1:1.8) at 900 MHz. In the same way, 1:7.8 variation of X_{Rect} results in 1:1.2 variation of real (Z_{in}). The observation from Fig. 13 is that the impedance variation with the rectifier stacking can be made less effective with the proper selection of matching network components.

IV. Measurement Results

To validate the proposed design, the multiband (GSM900, GSM1800, 4G-LTE, and Wi-Fi) harvester is fabricated on FR4 substrate (εr = 4.3 and thickness = 1.6 mm) using Schottky diodes (HSMS 2850) and passive SMD (Murata and Coilcraft) components, as shown in Fig. 14. Following this, a PMM module from TI (BQ25570) is used with 50% maximum power point tracking (MPPT) to boost the rectifier output voltage. To measure the harvester at multiple bands simultaneously, two 2-port E5080A ENA microwave network analyzer from Keysight is connected to an input of the power combiner ZFRSC-4-842+, as shown in Figs. 15 and 16. The measurements are taken after the calibration. A manual calibration kit 85056D has been used for the calibration of the ENA E5080A network analyzer with the short–open–load–thru (SOLT) technique. This calibration deembeds the parasitic effect of RF cable, SMA connector, and printed circuit board (PCB) trace up to the first component of matching network.

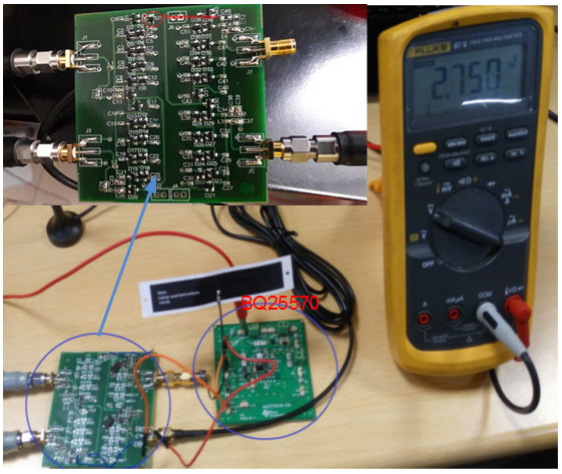

Fig. 14. Stacked rectifiers array fabricated on FR4 substrate, $\varepsilon_r = 4.3$ and thickness = 1.6 mm.

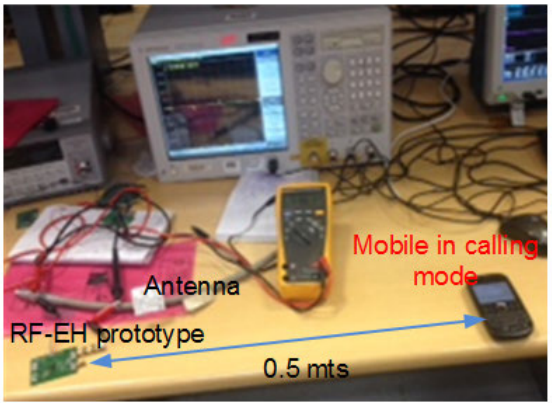

Fig. 15. Setup to measure the harvester module prototype.

In this design to limit the size, an inverted F antenna from Molex (series 146185) is chosen for measurements. The antenna measures 34.9 × 9 × 0.1 mm and has an efficiency and a peak gain of 75% and 4.5 dBi at 900 MHz, 62% and 4.7 dBi at 1.8 GHz, and 56% and 3.0 dBi at 2.3 GHz and 2.4 GHz, respectively. The antenna radiation pattern, gain, and efficiency at 0.9, 2.4 GHz is given in the Appendix. For the simulations, a sinusoidal port with a radiation resistance of 50 Ω is considered with an input power level range from −30 to 10 dBm.

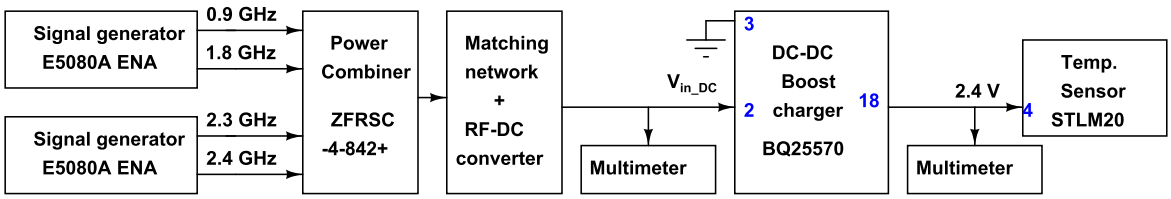

Fig. 16. Block diagram of test setup to measure prototype.

TABLE III
PERFORMANCE COMPARISON WITH RECENT LITERATURE

Ref.	Rectifier topology	No. of RF tones	RF bands (GHz)	Efficiency
[6]	Stacked	Multiband	0.9, 1.8, 2.1, 2.4	35.4% at -20 dBm
[9]	Half-wave rectifier	Dualband	0.915, 1.8	<30% at -15 to 20 dBm
[12]	Half-wave rectifier	4RF tones	0.5, 0.9, 1.8, 2.4	15% at -12 dBm
[10]	Half-wave rectifier	Multiband	0.9, 1.2, 2.0, 2.4	<30% at -12 to 12 dBm
[19]	Voltage doubler	5 RF tones	0.26, 0.4, 0.47, 0.9, 1.35	19, 20, 16, 17 and 5% at -10 dBm
[20]	Half-wave rectifier	1-RF tone	0.45	45% at -10 dBm
[21]	Half-wave rectifier	2-RF tones	0.9, 1.8	15% at -20 dBm
[22]	Half-wave rectifier	2-RF tones	0.91, 2.45	30% at -9 dBm
[28]	Half-wave rectifier	3-RF tones	1.85,2.15,2.48	33.4% at -14 dBm
[27]	Half-wave rectifier	8-RF tones	0.84, 1.29,1.68,3.08,3.45,4.31,5.11,5.49	38% at -14 dBm
[26]	Half-wave rectifier	7-RF tones	1.84,2.04,2.36,2.54,3.3,4.76,5.8	34.2% at -14 dBm
This work	Feedforward stacked	Multiband	0.9,1.8,2.3,2.4	44.2% at -20 dBm

Efficiency is the ratio of total output power at the rectifier output to the source power at the input of the matching network.

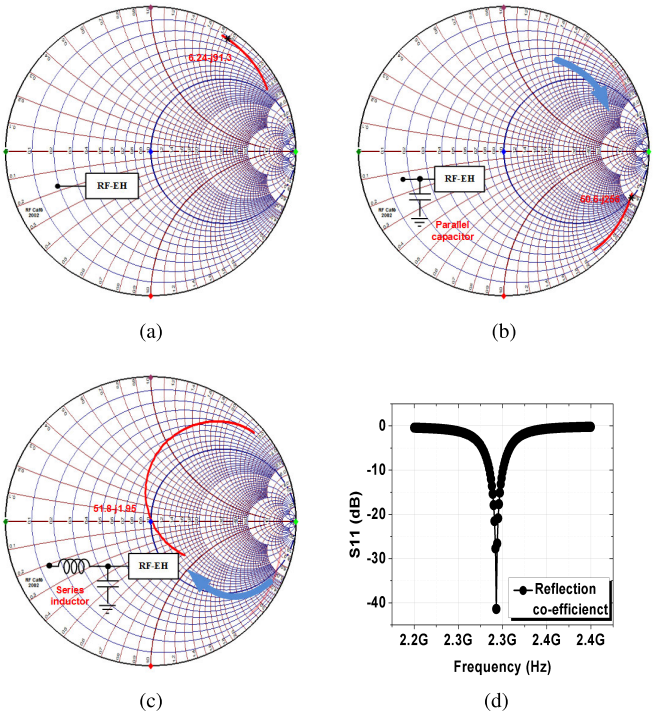

Fig. 17. (a) Impedance loci without matching network. (b) Impedance loci with parallel capacitor. (c) Impedance loci with series inductor and parallel capacitor. (d) S_{11} plot.

Design of Matching Network During Measurement: At simulation, the matching network is designed by calculating the impedance of the rectifier using HB analysis in Agilent ADS. However, the Smith chart is used during measurement to plot the complex impedance of the rectifier. The preliminary procedure for implementing the matching network at single frequency during measurement is shown in the following.

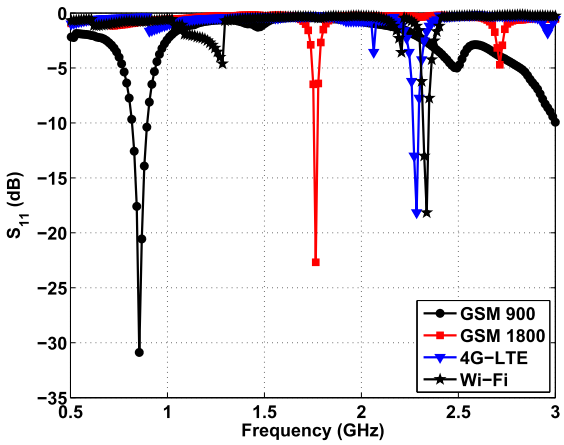

Fig. 18. Measured S_{11} of the RF harvester at $P_{\text{in}} = -10$ dBm and $R_L = 40$ KΩ.

1) *Step 1*: Determined the rectifier impedance at the desired frequency (2.3 GHz) using a network analyzer, as shown in Fig. 17(a). The impedance is $R_{\text{Rect}} - jX_{\text{Rect}}$ $(6.24 - j91.3)$, which falls on the capacitive side.
2) *Step 2*: Transformed the impedance to fall on either the 50-Ω circle or the 20-mS circle by placing capacitor (C_p) in parallel, as shown in Fig. 17(b). The transformed impedance is $Z_0 - jX_T = (50.6 - j256)$.
$Z_0 - jX_T = (R_{\text{Rect}} - jX_{\text{Rect}})||(-jX_{cp})$

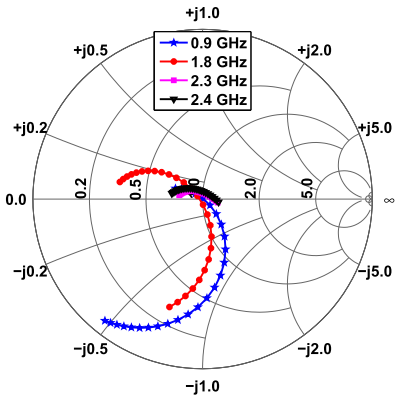

Fig. 19. Measured S_{11} of the RF harvester at $P_{in} = -10$ dBm and $R_L = 40$ KΩ.

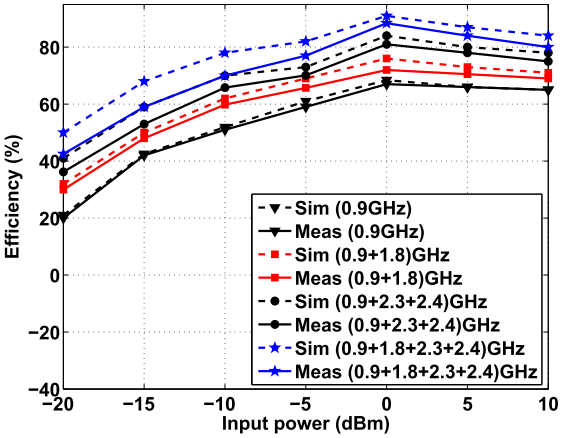

Fig. 20. Measured RF-to-dc Efficiency versus input power with one, two, three, or four continuous-wave RF signals at optimum load conditions. All bands are excited with the same power. The efficiency is calculated as η = (Harvested power/Input power at any frequency band) $*$ 100.

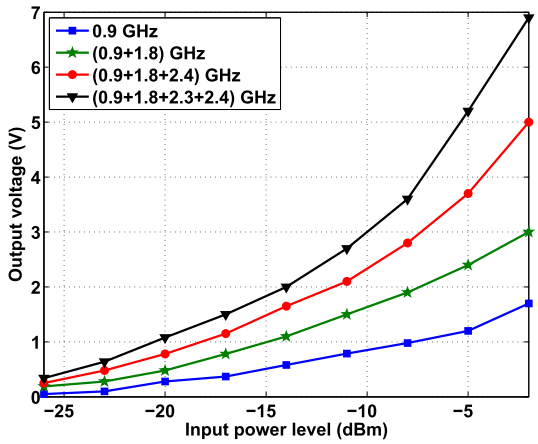

Fig. 21. Measured output voltage versus input power at $R_L = \infty$.

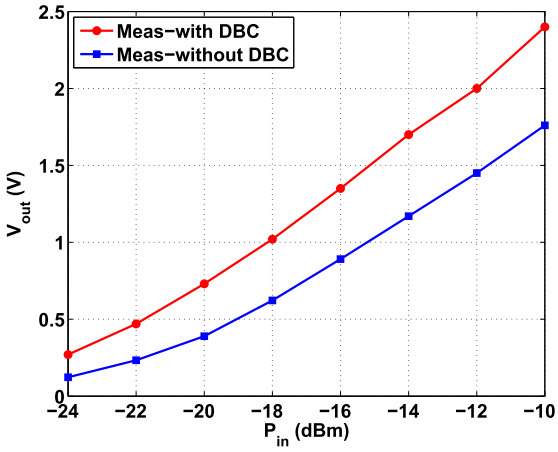

Fig. 22. Measured output voltage versus input power with one inactive band (f_2 = inactive and f_1, f_3, f_4 = active).

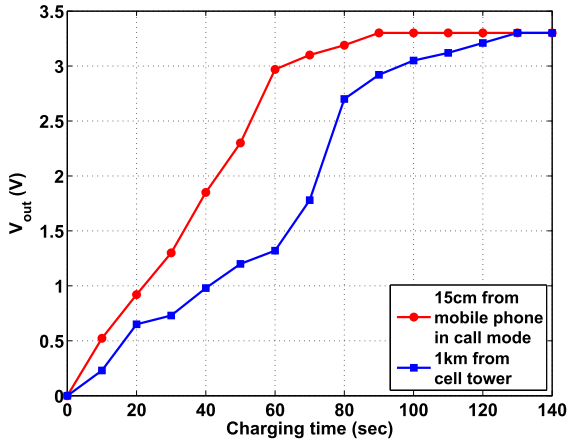

Fig. 23. Charging profile of a supercapacitor (BZ05FB682ZSB) of 6.8 mF.

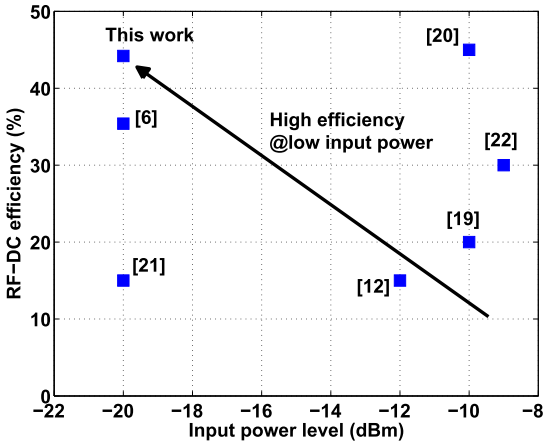

Fig. 24. Performance comparison with the existing literature.

3) *Step 3*: Moved the impedance from the 50-Ω circle to the 50-Ω point by connecting series inductor (L_s) as shown in Fig. 17(c) and the equivalent equation is given as: $Z_0 = Z_0 - jX_T + jX_{Ls}$ and $L_s = X_T/\omega$. The input port reflection coefficient S_{11} plot to this transformed impedance is given in Fig. 17(d).

At RF frequencies, the measured impedance changes with the distance from the SMA connector feed (where the input power is fed) to a rectifier. Impedance rotates around the characteristic impedance of the RF trace in a Smith chart clockwise when the SMA feed moves away from the rectifier. Thus, the matching network would need to change if the distance from the SMA connector feed to rectifier varies. Thus,

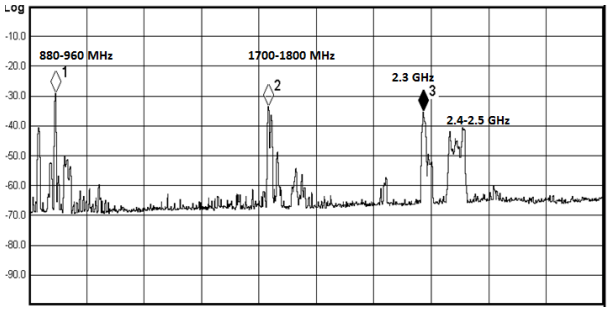

Fig. 25. RF power spectrum of an inverted F antenna from Molex (series 146185).

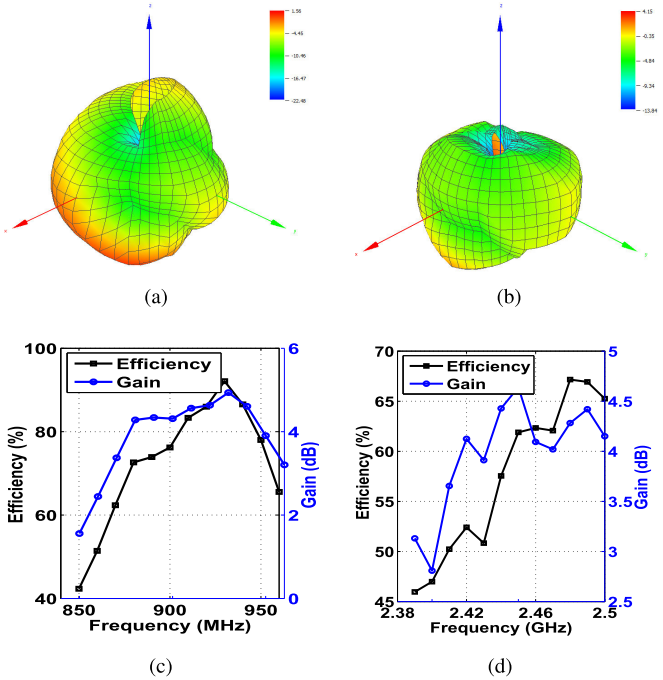

Fig. 26. Antenna radiation pattern, gain, and efficiency of antenna from Molex (series 146185) at (a) 900 MHz, (b) 2.4 GHz, (c) 900 MHz, and (d) 2.4 GHz.

the recommended technique is to place the matching network and rectifier circuit close to the SMA connector feed or the edge of the PCB board to avoid the PCB trace effects.

The S_{11} for all the frequency bands at −10-dBm input power level is shown in Figs. 18 and 19 and attained $S_{11} < -16$ dB in the desired frequencies. The measured power conversion efficiency as a function of input power is represented in Fig. 20 and observed the increment in the efficiency with the number of bands. This shows the peak efficiencies of 89% and 44.2% at 0- and −20-dBm input powers with the four-RF bands, respectively. The output voltage as a function of input power at multiple RF bands is shown in Fig. 21. With the proposed stage–stage feedforward technique, this improves the efficiency by 5%/9% at 0/−20 dBm compared to [6], which implicitly implies the improvement in the minimum sensitivity. Furthermore, Fig. 22 shows the improvement in the output voltage (0.3/0.5 V at −20/−18 dBm) of the harvester by introducing DBC.

Furthermore, Fig. 23 shows the charged profile of output supercapacitor of BQ25570 under the near-/far-field radiation circumstance in a real field using a quad-band antenna from Molex (series 146185). Finally, the full system drives a temperature sensor STLM20 at −3-/−8-/−12-dBm input power in the presence of two/three/four RF bands, and the output voltage of STLM20 is 1.2 V (25 °C) at −12-dBm input power. Performance comparisons with the prior literature are shown in Fig. 24 and Table III.

V. Conclusion

A stage–stage feedforward multiband stacked RF-EH is proposed to reach the lowest possible ambient input RF power levels and to extend the harvesting range. This multiband series topology with a DBC network has been designed and fabricated to cover the GSM900, GSM1800, 4G-LTE, and Wi-Fi RF bands. It shows a cumulative conversion efficiency of 89% and 44.2% at 0- and −20-dBm input power, respectively. This multiband voltage summing array architecture achieved at an input RF power level as low as −24 dBm to cold-start the PMM, without any external power supply. Furthermore, the proposed works are achieving closer to the ambient received power levels and are able to drive a temperature sensor STLM20 at −12-dBm input power.

VI. Future Scope

There is a lot of potential for RF energy harvesting for applications of the Internet-of-Things (IoT) and home automation projects. Smart sensor technology is capable of producing low-power devices with advanced embedded technology, which typically operates at microwatt input power. Wireless sensors for temperature, humidity, and proximity sensors are used in the industrial, home automation, and automobile industry. Wire-free charging of any electronic device would be possible with the multiband RF energy harvesting technology.

Appendix

The solution for L_R and C_R is obtained by solving (17)

$$\left(1+\frac{1}{Q_L^2}\right)R_{\text{Rect}}X_{L_R}^2+\left(\left(\frac{1}{Q_L}+\frac{1}{Q_C}\right)R_{\text{Rect}}^2-\frac{2R_iR_{\text{Rect}}}{Q_L}\right)\times X_{L_R}+R_iR_{\text{Rect}}(R_i-R_{\text{Rect}})=0. \tag{24}$$

$$(1+Q_C^2)(R_{\text{Rect}}-R_i)X_{C_R}^2+R_{\text{Rect}}Q_C\times\left(\frac{R_{\text{Rect}}Q_C}{Q_L}+R_{\text{Rect}}-2R_i\right)X_{C_R}-R_iR_{\text{Rect}}^2Q_C^2=0. \tag{25}$$

The solutions for L_L and C_L are obtained by solving $\text{real}(Z_{\text{in}_L})=R_S$ and $\text{imag}(Z_{\text{in}_L})=0$

$$\left(1+\frac{1}{Q_L^2}\right)X_{L_L}^2+\frac{2R_i-R_S}{Q_L}X_{L_L}+R_i^2\sqrt{\frac{R_S}{R_i}-1}=0. \tag{26}$$

$$(R_S-R_i)\left(1+\frac{1}{Q_C^2}\right)X_{C_L}^2+\left(\frac{2R_SR_i}{Q_C}-R_S^2\left(\frac{1}{Q_L}+\frac{1}{Q_C}\right)\right)\times X_{C_L}-R_S^2R_i=0. \tag{27}$$

ACKNOWLEDGMENT

The authors would like to thank Intel Technology India Pvt. Ltd for their constructive support during testing.

REFERENCES

[1] F. Deng, X. Yue, X. Fan, S. Guan, Y. Xu, and J. Chen, "Multisource energy harvesting system for a wireless sensor network node in the field environment," *IEEE Internet Things J.*, vol. 6, no. 1, pp. 918–927, Feb. 2019, doi: 10.1109/JIOT.2018.2865431.

[2] V. Leonov, T. Torfs, R. J. M. Vullers, and C. Van Hoof, "Hybrid thermoelectric–photovoltaic generators in wireless electroencephalography diadem and electrocardiography shirt," *J. Electron. Mater.*, vol. 39, no. 9, pp. 1674–1680, Apr. 2010.

[3] P. Nintanavongsa et al., "Design optimization and implementation for RF energy harvesting circuits," *IEEE J. Emerg. Sel. Topics Circuits Syst.*, vol. 2, no. 1, pp. 24–33, Mar. 2012.

[4] W. Huang, B. Zhang, X. Chen, K.-M. Huang, and C.-J. Liu, "Study on an S-band rectenna array for wireless microwave power transmission," *Prog. Electromagn. Res.*, vol. 135, pp. 747–758, 2013.

[5] C. Mikeka, H. Arai, A. Georgiadis, and A. Collado, "DTV band micropower RF energy-harvesting circuit architecture and performance analysis," in *Proc. IEEE Int. Conf. RFID-Technol. Appl.*, Sep. 2011, pp. 561–567.

[6] V. Kuhn et al., "A multi-band stacked RF energy harvester with RF-to-DC efficiency up to 84%," *IEEE Trans. Microw. Theory Techn.*, vol. 63, no. 5, pp. 1768–1778, May 2015.

[7] J. A. Hagerty, F. B. Helmbrecht, W. H. McCalpin, R. Zane, and Z. B. Popovic, "Recycling ambient microwave energy with broad-band rectenna arrays," *IEEE Trans. Microw. Theory Techn.*, vol. 52, no. 3, pp. 1014–1024, Mar. 2004.

[8] U. Muncuk, K. Alemdar, J. D. Sarode, and K. R. Chowdhury, "Multi-band ambient RF energy harvesting circuit design for enabling batteryless sensors and IoT," *IEEE Internet Things J.*, vol. 5, no. 4, pp. 2700–2714, Aug. 2018.

[9] Z. Liu, Z. Zhong, and Y.-X. Guo, "Enhanced dual-band ambient RF energy harvesting with ultra-wide power range," *IEEE Microw. Wireless Compon. Lett.*, vol. 25, no. 9, pp. 630–632, Sep. 2015.

[10] J.-J. Lu, X.-X. Yang, H. Mei, and C. Tan, "A four-band rectifier with adaptive power for electromagnetic energy harvesting," *IEEE Microw. Wireless Compon. Lett.*, vol. 26, no. 10, pp. 819–821, Oct. 2016.

[11] C.-Y. Hsu, S.-C. Lin, and Z.-M. Tsai, "Quadband rectifier using resonant matching networks for enhanced harvesting capability," *IEEE Microw. Wireless Compon. Lett.*, vol. 27, no. 7, pp. 669–671, Jul. 2017.

[12] M. Pinuela, P. D. Mitcheson, and S. Lucyszyn, "Ambient RF energy harvesting in urban and semi-urban environments," *IEEE Trans. Microw. Theory Techn.*, vol. 61, no. 7, pp. 2715–2726, Jul. 2013.

[13] H. Sun, Z. Zhong, and Y.-X. Guo, "An adaptive reconfigurable rectifier for wireless power transmission," *IEEE Microw. Wireless Compon. Lett.*, vol. 23, no. 9, pp. 92–94, Sep. 2013.

[14] P. Soboll, V. Wienstroer, and R. Kronberger, "Stacked Yagi–Uda array for 2.45-GHz wireless energy harvesting," *IEEE Microw. Mag.*, vol. 16, no. 1, pp. 67–73, Feb. 2015.

[15] Z. Popović et al., "Scalable RF energy harvesting," *IEEE Trans. Microw. Theory Techn.*, vol. 62, no. 4, pp. 1046–1056, Apr. 2014.

[16] F. Xie, G.-M. Yang, and W. Geyi, "Optimal design of an antenna array for energy harvesting," *IEEE Antennas Wireless Propag. Lett.*, vol. 12, pp. 155–158, 2013.

[17] S. D. Assimonis, S.-N. Daskalakis, and A. Bletsas, "Efficient RF harvesting for low-power input with low-cost lossy substrate rectenna grid," in *Proc. IEEE RFID Technol. Appl. Conf. (RFID-TA)*, Sep. 2014, pp. 1–6.

[18] J. A. Hagerty, F. B. Helmbrecht, W. H. McCalpin, R. Zane, and Z. B. Popovic, "Recycling ambient microwave energy with broad-band rectenna arrays," *IEEE Trans. Microw. Theory Techn.*, vol. 52, no. 3, pp. 1014–1024, Mar. 2004.

[19] A. N. Parks and J. R. Smith, "Sifting through the airwaves: Efficient and scalable multiband RF harvesting," in *Proc. IEEE Int. Conf. RFID (IEEE RFID)*, Apr. 2014, pp. 74–81.

[20] A. Collado and A. Georgiadis, "Optimal waveforms for efficient wireless power transmission," *IEEE Microw. Wireless Compon. Lett.*, vol. 24, no. 5, pp. 354–356, May 2014.

[21] A. Collado and A. Georgiadis, "Conformal hybrid solar and electromagnetic (EM) energy harvesting rectenna," *IEEE Trans. Circuits Syst. I, Reg. Papers*, vol. 60, no. 8, pp. 2225–2234, Aug. 2013.

[22] K. Niotaki, S. Kim, S. Jeong, A. Collado, A. Georgiadis, and M. M. Tentzeris, "A compact dual-band rectenna using slot-loaded dual band folded dipole antenna," *IEEE Antennas Wireless Propag. Lett.*, vol. 12, pp. 1634–1637, 2013.

[23] (2019). *Ultra-low Current 2.4 V Precision Analog Temperature Sensor*. [Online]. Available: https://www.st.com/resource/en/datasheet/stlm20.pdf

[24] (2020). *Integrated Pressure, Temperature & Humidity Sensor MS8607*. [Online]. Available: https://www.servoflo.com/download-archive/datasheets/256-humidity/1140-ms8607-02ba01-datasheet

[25] (2019). *High Performance Digital Temperature Sensor*. [Online]. Available: https://www.servoflo.com/images/PDF/mvt3000d.pdf

[26] Y. Wang et al., "Efficiency enhanced seven-band omnidirectional rectenna for RF energy harvesting," *IEEE Trans. Antennas Propag.*, vol. 70, no. 9, pp. 8473–8484, Sep. 2022, doi: 10.1109/TAP.2022.3177492.

[27] N. Mirzababaee, F. Geran, and S. Mohanna, "A radio frequency energy harvesting rectenna for GSM, LTE, WLAN, and WiMAX," *Int. J. RF Microw. Comput.-Aided Eng.*, vol. 55, no. 2, pp. 35–42, Mar. 2021.

[28] S. Shen, Y. Zhang, C.-Y. Chiu, and R. Murch, "A triple-band high-gain multibeam ambient RF energy harvesting system utilizing hybrid combining," *IEEE Trans. Ind. Electron.*, vol. 67, no. 11, pp. 9215–9226, Nov. 2020.

S. Nagaveni received the master's and Ph.D. degrees in microelectronics and VLSI from the Indian Institute of Technology Hyderabad, Hyderabad, India, in 2014 and 2021 respectively.

From 2016 to 2017, she was a Graduate Intern with Intel Technology India Pvt. Ltd, Bangalore, India. From 2018 to 2021, she was at Sankalp Semiconductor (HCL Technology), Bangalore, as an Analog Design Engineer. She is presently working as an Assistant Professor with the Department of Electrical Engineering, Indian Institute of Technology Dharwad, Dharwad, India.

Sesha Sairam Regulagadda received the Ph.D. degree in microelectronics and VLSI from the Indian Institute of Technology Hyderabad, Hyderabad, India, in 2019.

He is presently working as a Senior RF Design Engineer at Silicon Labs, Hyderabad. His current research focuses on the design of reconfigured radio front ends for the Internet-of-Things (IoT) applications and the development of radio frequency (RF) circuits for defense applications.

Ashudeb Dutta (Member, IEEE) received the Ph.D. degree from the Department of Electronics and Electrical Communication Engineering, IIT Kharagpur, Kharagpur, India.

He is currently an Associate Professor with the Indian Institute of Technology Hyderabad (IIT Hyderabad), Hyderabad, India. He is also the Founding Director of Lemon Flip Solution Pvt. Ltd. and IIT Hyderabad. His research interests include analog circuits, radio frequency integrated circuit (RFIC), semiconductor devices, energy harvesting, biomedical and healthcare, and smart security.